

The role of environment in galaxy evolution in the SERVS survey I: density maps and cluster candidates

Article (Published Version)

Krefting, Nick, Sajina, Anna, Lacy, Mark, Nyland, Kristina, Farrah, Duncan, Darvish, Behnam, Duivenvoorden, Steven, Duncan, Ken, Gonzalez-Perez, Violeta, Lagos, Claudia Del P, Oliver, Seb, Shirley, Raphael and Vaccari, Mattia (2020) The role of environment in galaxy evolution in the SERVS survey I: density maps and cluster candidates. *Astrophysical Journal*, 889 (185). pp. 1-28. ISSN 0004-637X

This version is available from Sussex Research Online: <http://sro.sussex.ac.uk/id/eprint/88689/>

This document is made available in accordance with publisher policies and may differ from the published version or from the version of record. If you wish to cite this item you are advised to consult the publisher's version. Please see the URL above for details on accessing the published version.

Copyright and reuse:

Sussex Research Online is a digital repository of the research output of the University.

Copyright and all moral rights to the version of the paper presented here belong to the individual author(s) and/or other copyright owners. To the extent reasonable and practicable, the material made available in SRO has been checked for eligibility before being made available.

Copies of full text items generally can be reproduced, displayed or performed and given to third parties in any format or medium for personal research or study, educational, or not-for-profit purposes without prior permission or charge, provided that the authors, title and full bibliographic details are credited, a hyperlink and/or URL is given for the original metadata page and the content is not changed in any way.



The Role of Environment in Galaxy Evolution in the SERVS Survey. I. Density Maps and Cluster Candidates

Nick Krefting¹, Anna Sajina¹ , Mark Lacy² , Kristina Nyland³, Duncan Farrah^{4,5} , Behnam Darvish⁶ , Steven Duivenvoorden⁷, Ken Duncan⁸ , Violeta Gonzalez-Perez^{9,10}, Claudia del P. Lagos^{11,12,13}, Seb Oliver⁷ , Raphael Shirley^{7,14,15}, and Mattia Vaccari^{16,17}

¹ Department of Physics and Astronomy, Tufts University, 574 Boston Avenue, Medford, MA 02155, USA; nicholas.krefting@tufts.edu

² National Radio Astronomy Observatory, 520 Edgemont Road, Charlottesville, VA 22903, USA

³ National Research Council, resident at the Naval Research Laboratory, Washington, DC 20375, USA

⁴ Department of Physics and Astronomy, University of Hawaii, 2505 Correa Road, Honolulu, HI 96822, USA

⁵ Institute for Astronomy, 2680 Woodlawn Drive, University of Hawaii, Honolulu, HI 96822, USA

⁶ California Institute of Technology, Pasadena, CA 91125, USA

⁷ Astronomy Centre, Department of Physics and Astronomy, University of Sussex, Brighton BN1 9QH, UK

⁸ Leiden Observatory, Leiden University, P.O. Box 9513, NL-2300 RA Leiden, The Netherlands

⁹ Astrophysics Research Institute, Liverpool John Moores University, 146 Brownlow Hill, Liverpool L3 5RF, UK

¹⁰ Institute of Cosmology & Gravitation, University of Portsmouth, Dennis Sciana Building, Portsmouth, PO1 3FX, UK

¹¹ International Centre for Radio Astronomy Research (ICRAR), M468, University of Western Australia, 35 Stirling Highway, Crawley, WA 6009, Australia

¹² ARC Centre of Excellence for All Sky Astrophysics in 3 Dimensions (ASTRO 3D), Australia

¹³ Cosmic Dawn Center (DAWN), Copenhagen, DK-0000-0003-3631-7176, Denmark

¹⁴ Instituto de Astrofísica de Canarias, E-38205 La Laguna, Tenerife, Spain

¹⁵ Dpto. Astrofísica, Universidad de La Laguna, E-38206 La Laguna, Tenerife, Spain

¹⁶ Department of Physics and Astronomy, University of the Western Cape, Private Bag X17, Bellville 7535, South Africa

¹⁷ INAF—Istituto di Radioastronomia, via Gobetti 101, I-40129 Bologna, Italy

Received 2019 June 19; revised 2019 November 8; accepted 2019 November 18; published 2020 February 5

Abstract

We use photometric redshifts derived from new u -band through $4.5\ \mu\text{m}$ *Spitzer* IRAC photometry in the $4.8\ \text{deg}^2$ of the *XMM*-LSS field to construct surface density maps in the redshift range of 0.1–1.5. Our density maps show evidence for large-scale structure in the form of filaments spanning several tens of megaparsecs. Using these maps, we identify 339 overdensities that our simulated light-cone analysis suggests are likely associated with dark matter halos with masses, $M_{\text{halo}}, \log(M_{\text{halo}}/M_{\odot}) > 13.7$. From this list of overdensities we recover 43 of 70 known X-ray-detected and spectroscopically confirmed clusters. The missing X-ray clusters are largely at lower redshifts and lower masses than our target $\log(M_{\text{halo}}/M_{\odot}) > 13.7$. The bulk of the overdensities are compact, but a quarter show extended morphologies that include likely projection effects, clusters embedded in apparent filaments, and at least one potential cluster merger (at $z \sim 1.28$). The strongest overdensity in our highest-redshift slice (at $z \sim 1.5$) shows a compact red galaxy core, potentially implying a massive evolved cluster.

Unified Astronomy Thesaurus concepts: Galaxy clusters (584); Redshift surveys (1378); Large-scale structure of the universe (902); Galaxy cluster counts (583)

Supporting material: machine-readable table

1. Introduction

Many studies over the past few decades have shown that the local density in which a galaxy resides affects its growth, quenching, and morphology (e.g., Cochrane & Best 2018). The physical mechanisms through which the environment plays a role include gas accretion, feedback, and galaxy interactions. At low redshift, this environmental dependence is well known, with “red and dead” elliptical galaxies dominating in denser environments, while star-forming spirals are more commonly found in the field (e.g., Dressler 1980; Norberg et al. 2002; Peng et al. 2010). Higher- z studies also show environmental trends such as the faster buildup and quenching of more massive galaxies in denser environments (e.g., van der Burg et al. 2013; Etherington et al. 2017) and more generally the dependence of the specific star formation rate (SFR) on local environment (e.g., Duivenvoorden et al. 2016) and large-scale environment such as proximity to a filament (Malavasi et al. 2017; Laigle et al. 2018).

To help elucidate the mechanisms through which the environment affects galaxy and black hole evolution, we need surveys that reach high enough redshift to sample the epochs where the bulk of

the stellar and black hole masses were assembled (the bulk of stellar mass growth happened at $z \sim 0.5$ –2; Madau & Dickinson 2014). We also need a large enough volume to sample a representative range of environments with good statistics. Spectroscopic surveys are ideal because of their ability to localize galaxies in 3D precisely; however, they do not reach to high enough redshift with high enough sampling rates (see, e.g., the VIMOS Public Extragalactic Redshift survey [VIPERS], for state of the art; Guzzo et al. 2014) and tend to be biased against redder galaxies by selection. High-quality photometric redshifts can work as shown for the COSMOS survey (e.g., Darvish et al. 2015a; Laigle et al. 2016), but, with an area of only $2\ \text{deg}^2$, this survey is not quite a representative cosmic volume and suffers from significant cosmic variance and poor statistics at the high-mass end (Moster et al. 2011; Darvish et al. 2015a; Yang et al. 2018).

The *Spitzer* Extragalactic Representative Volume Survey (SERVS; see Mauduit et al. 2012, for survey definition and early results) was designed specifically to address these issues. With a total volume of $\approx 1\ \text{Gpc}^3$ out to $z \sim 3$, this survey reaches galaxies down to stellar masses of $M_* \sim 10^{9.5} M_{\odot}$ at $z \sim 2$, corresponding to the epoch of “cosmic noon,” and

probes the full range of environments from voids to massive clusters. The survey centers on the *Spitzer* IRAC data, which sample the rest-frame near-IR out to cosmic noon and therefore allow for accurate stellar parameter estimation (Muzzin et al. 2009). The full multiwavelength coverage, spanning from the X-rays to the radio, allows us to derive accurate photometric redshifts, SFRs, and active galactic nucleus (AGN) presence and strength for our galaxies. In a series of papers, we use the SERVS and ancillary data to explore the role of environment in galaxy and black hole evolution.

In this first paper of the series, we construct 2D density maps for the 4.8 deg^2 *XMM*-LSS field, where we have the most uniform and deep multiwavelength coverage in hand. The *XMM*-LSS field is already $2.5\times$ the size of COSMOS, with ≈ 300 dark matter halos with $\log(M_{\text{halo}}/M_{\odot}) > 13.7$. The existing massive halo catalogs in this field are the X-ray cluster catalogs (Clerc et al. 2014; Adami et al. 2018). Our density maps allow us to construct an independent and complementary catalog of the massive halos in this field. This is because our catalog has a redshift-independent halo mass limit, whereas X-ray cluster selection has a strong redshift dependence of its limiting mass. In addition, density maps allow us to find overdensities that are not yet virialized, X-ray-emitting halos. This paper is also a test case of what we can do with the quality of photometric data that are expected in the near future for a total of $\approx 15 \text{ deg}^2$ spread across four fields with matching coverage from the u band through the mid-IR. We demonstrate our ability to recover the highest-density peaks and even pick up some large-scale-structure-like filaments. We stress, however, that, being based on photometric redshifts, our overdensities are only candidates. They require spectroscopic confirmation. This should be available for many of these overdensities in the near future since this field is also covered by the ongoing DEVILS and the upcoming Prime Focus Spectrograph (PFS) spectroscopic surveys (Davies et al. 2018; Tanaka et al. 2018), which will significantly increase the spectroscopic coverage of the field out to cosmic noon.

This paper is organized as follows. In Section 2 we discuss the photometric and spectroscopic data in the *XMM*-LSS field. We also discuss the light cone of simulated galaxies we use to help us interpret our observational results. In Section 3, we present our analysis. This includes photometric redshift determination and uncertainty estimates, as well as density map generation in the simulated and observed data set. We present a list of 339 overdensity-selected cluster candidates and compare them with catalogs of spectroscopically confirmed X-ray clusters in the field. In Section 4, we give our summary and conclusions. Throughout this paper, we adopt the Planck2015 cosmology (Planck Collaboration et al. 2016), such that $\Omega_m = 0.3075$, $\Omega_{\Lambda} = 0.691$, and $H_0 = 67.74 \text{ km s}^{-1} \text{ Mpc}^{-1}$. All magnitudes are in the AB system.

2. Data

2.1. Photometry

Our photometric data rely on the multiwavelength coverage of SERVS, which provides *Spitzer* IRAC 3.6 and $4.5 \mu\text{m}$ data of a depth sufficient to reach below M_* (based on the compilation in Madau & Dickinson 2014) at cosmic noon across an area wide enough to cover a representative volume of the universe. Specifically, it reaches a 5σ point-source depth of $\approx 2 \mu\text{Jy}$ ($AB = 23.1$) and covers 18 deg^2 spread across five fields to combat cosmic variance (see Moster et al. 2011). Each

field has an area of $\sim 2\text{--}5 \text{ deg}^2$, which allows for large extended structures such as protoclusters and filamentary networks to be studied (Yamada et al. 2012; Chiang et al. 2017).

In this paper we focus on the *XMM*-LSS field, for which a new multiband photometric catalog has been constructed using forced photometry (Nyland et al. 2017; K. Nyland et al. 2020, in preparation). This catalog was constructed using the Tractor code (Lang et al. 2016) and uses one image as a reference for the source model, which includes positions and surface brightness profiles of galaxies. The VIDEO K_s band is the preferred reference image for the bulk of the galaxies, but other bands are used under certain circumstances, such as gaps in coverage. These source models are applied across all other bands. This method is particularly crucial for deblending the IRAC 3.6 and $4.5 \mu\text{m}$ photometry. We use this catalog for the u -band through $4.5 \mu\text{m}$ photometry. For the longer-wavelength photometry, including IRAC 5.8 and $8.0 \mu\text{m}$ and MIPS $24 \mu\text{m}$ (from SWIRE; Lonsdale et al. 2003) and *Herschel* SPIRE 250, 350, and $500 \mu\text{m}$ photometry, we use the band-merged catalog published by the *Herschel* Extragalactic Legacy Program (HELP; Vaccari 2016; Shirley et al. 2019).¹⁸ The HELP team also has published photometric redshifts in the field (Duncan et al. 2018), but this is based on their band-merged catalog (R. Shirley et al. 2020, in preparation), as opposed to the forced photometry catalog described above. We compare our photometric redshifts (derived below) with the HELP photometric redshifts. We find them to be consistent out to $z \sim 1$; however, our IRAC deblending (thanks to the forced photometry catalog) leads to more accurate redshifts at $z \sim 1\text{--}2$. Therefore, in this paper we use our own photometric redshift estimates. Since Duncan et al. (2018) use AGN templates in their photo- z analysis, for the objects flagged as AGNs (see below), we adopt the Duncan et al. (2018) photometric redshifts for AGNs. We also use the spectroscopic redshifts and quality flags (see below) as compiled in the HELP catalog.¹⁹

In the 4.8 deg^2 *XMM*-LSS field, there are ~ 1.25 million objects. We remove stars by using the Baldry et al. (2010) $J\text{--}K_s$ versus $g\text{--}i$ color cut, leaving us with ~ 1.09 million nonstellar objects (see Figure 1). In the right panel of Figure 1 we plot the differential K_s -band number counts in the field using Tractor photometry and compare them with the counts using the VIDEO photometry from Jarvis et al. (2013). Tractor measures flux by fitting a surface brightness profile, whereas Jarvis et al. (2013) use a fixed aperture. Tractor thus collects more flux from brighter, extended sources, accounting for the discrepancy between the two number counts at brighter magnitudes. We also overlay the counts from our simulated light cone (see below for details). This light cone assumes the original depth of SERVS in the IRAC bands (see Mauduit et al. 2012), which leads to significant incompleteness above $K_s \sim 23$. Our current Tractor photometry, which uses the K_s image as a reference, has allowed us to reach below the original single-band-based photometry of SERVS. Since we rely on our simulated light cone for analysis, though, we limit our sample to $K_s < 23$ to ensure a closer comparison. This yields 441,969 galaxies. We finally remove 16,211 additional objects classified as stars in the Sloan Digital Sky Survey (SDSS) (but missed in Figure 1). This leads to a final sample of 425,758 galaxies.

In this sample we also flag any AGN that we select based on (a) X-ray counterpart (based on the Chen et al. 2018 catalog),

¹⁸ <http://hedam.lam.fr/HELP>

¹⁹ See also: <http://www.mattivaccari.net/df/specz/>.

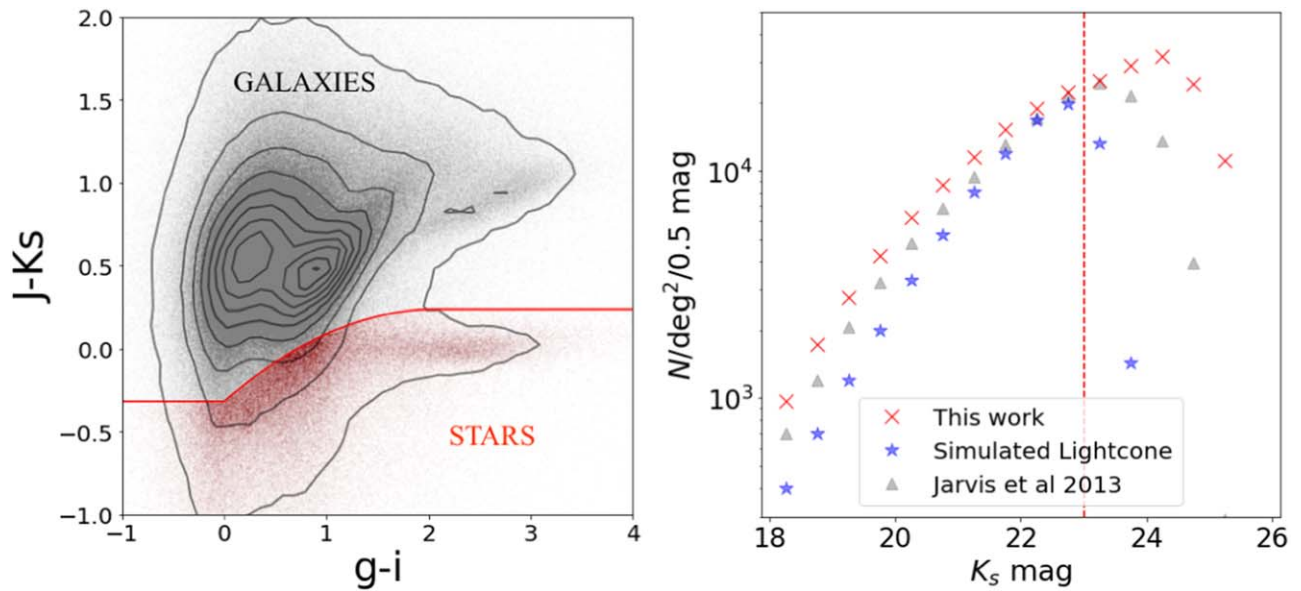


Figure 1. Left: separation of stars and galaxies using the $J-K_s$ vs. $g-i$ color cut described in Baldry et al. (2010). Right: differential K_s number counts after star removal. The counts from Jarvis et al. (2013) are included for reference. The red dashed line indicates the K_s magnitude limit of 23, which we adopt for this work for consistency with the simulated light cone (note that our light cone is constructed based on a $3.6\ \mu\text{m}$ limited sample, not a K_s -limited one).

(b) having AGN-like mid-IR colors, or (c) being spectroscopically classified as an AGN in SDSS, leading to a total of 2113 potential AGNs. AGNs are not removed from the sample because we are interested in the effect of environment on the incidence, type, and strength of the AGN. However, given their typically significantly more uncertain redshifts, we exclude them in the redshift quality assessment shown in Section 3.1 and the density map determinations in Section 3. Because the number of AGNs is so small, this has a negligible effect on our results.

2.2. Spectroscopic Data

The *XMM*-LSS field has significant spectroscopic redshift coverage. This is primarily from the VIMOS VLT Deep Survey (VVDS; Le Fèvre et al. 2013) and the VIMOS Ultra-Deep Survey (VUDS; Le Fèvre et al. 2015). The VVDS and VUDS are i -band-magnitude-selected surveys, going down to $i_{AB} = 24$ and $i_{AB} \simeq 25$, respectively. These data are complemented by the VIPERS (Guzzo et al. 2014) down to $i_{AB} = 22.5$, the PRISM Multi-object Survey (PRIMUS; Coil et al. 2011; Cool et al. 2013) down to $i_{AB} = 23$, the SDSS (Alam et al. 2015) down to $i_{AB} = 21.3$, the UKIDSS Ultra-Deep Survey (UDSz; Bradshaw et al. 2013; McLure et al. 2013) down to $i_{AB} = 25$, and the Australian Dark Energy Survey (OzDES; Yuan et al. 2015) down to $r_{AB} = 25$. Note that these do not all cover the full area, and targeted campaigns, such as for cluster confirmation in the field (see, e.g., Adami et al. 2018), are not included. These spectroscopic data are compiled as part of HELP and documented on their website.²⁰ We also supplement with redshifts from the VANDELS survey (McLure et al. 2018; Pentericci et al. 2018), which uses the VIMOS spectrograph down to a limit of $i_{AB} = 27.5$. In total, 76,016 sources in our sample have spectroscopic redshifts available in the *XMM*-LSS, 16,342 of which have been flagged as $>99\%$ reliable in the HELP catalog. This represents 3.7% of our sample.

²⁰ <http://hedam.lam.fr/HELP>

2.3. Simulated Data

To assess the reliability of environment measures in the presence of photometric redshift uncertainties, we employ a simulated catalog designed to cover an area and volume equivalent to the SERVS survey. Our simulated data are built from the Millennium N -body simulation (Springel 2005). Model galaxies were constructed using the Lagos12 GALFORM semianalytic model (Cole et al. 2000; Lagos et al. 2012) using the method described in Merson et al. (2013). GALFORM models the main physical processes of galaxy formation and evolution, using the formation histories of dark matter halos as a starting point. Our light cone covers 18 deg^2 and spans the redshift range $0.0 < z < 6.0$, containing 1,518,854 galaxies.²¹ This translates to $\approx 400,000$ in a 4.8 deg^2 field, consistent with our data (after the $K_s < 23$ cut). Galaxy stellar mass and parent halo mass are both outputs of the light cone. We also have simulated observations of each galaxy in the SDSS z band, the DECam Y band, and the UKIRT J , H , K , and K_s bands. The cosmology of the simulated light cone is different from that which we assume for our observed sample, but we correct for this by multiplying masses by the value of h appropriate to each sample.

3. Analysis

3.1. Photometric Redshifts

Only $\sim 4\%$ of the sources in the field have spectroscopic redshifts (Section 2.2), so we need photometric redshifts in order to trace the galaxy density field. We determine photometric redshifts using the EAZY code (Brammer et al. 2008).²² EAZY compares input photometry to a linear combination of template spectral

²¹ This light cone is publicly available on Zenodo (doi:10.5281/zenodo.3568147).

²² There are many choices here. The fact that we see comparable σ_{NMAD} and no significant systematic biases between our photometric redshifts and those derived for the same data set but using different models by Pforr et al. (2019) suggests that our results are likely robust against photometric redshift code systematics.

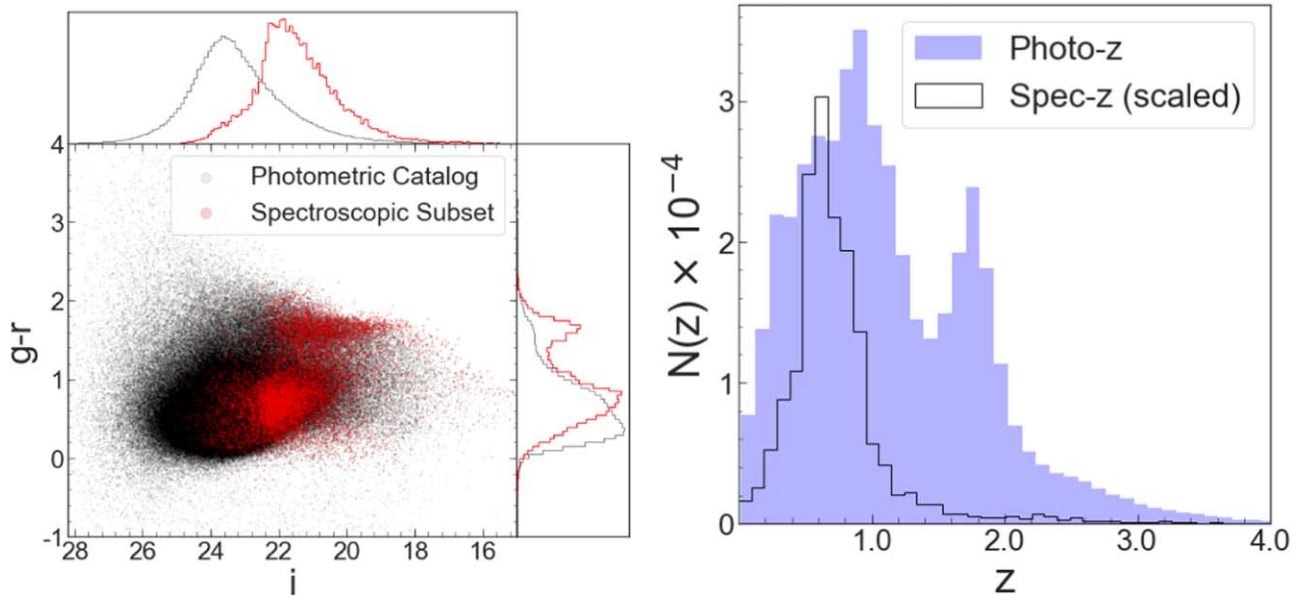


Figure 2. Left: $g-r$ color vs. i -band magnitude for our sample. The black points and histograms represent all galaxies in our sample, while the red points and histograms represent just those galaxies for which we have high-quality spec- z 's as defined in the text. Right: the photo- z distribution of our sample is shown (scaled as indicated) as the filled blue histogram. The spec- z distribution (scaled for comparison) is plotted as the open histogram.

Table 1
Systematic Offsets ($\text{mag}_{\text{data}} - \text{mag}_{\text{template}}$) for Each Filter Used to Calculate Photometric Redshifts in the *XMM*-LSS Catalog

Filter	OffsetWide	OffsetDeep	OffsetUltradeep	Filter	OffsetWide	OffsetDeep	OffsetUltradeep
u^*	0.2748	0.2372	0.2472	J	0.1235	0.0894	0.1475
g	-0.0031	-0.0848	-0.0742	H	0.0417	0.0024	0.0370
r	-0.0161	-0.2028	-0.0610	K_s	-0.1102	-0.1433	-0.1131
i	-0.0534	0.0440	-0.0111	[3.6]	0.0207	0.0156	0.0016
z	-0.0701	0.0662	-0.0245	[4.5]	-0.0029	-0.0016	-0.0031
y	0.0306	0.0337	-0.0084

energy distributions realized across a range of redshifts, returning the redshift of the combination giving the smallest χ^2 value and a redshift probability distribution function $p(z)$ for each galaxy. We use the EAZY template library including emission lines and a dusty star-forming template. We evaluate using the EAZY default redshift range $0 < z < 8$ in steps of $0.01(1+z)$.

We employ an iterative zero-point correction algorithm (see Brodwin et al. 2006; Ilbert et al. 2006) to correct for systematic magnitude deviations between the template set and our photometry. Here we restrict ourselves to those galaxies with high-quality spectroscopic redshifts for efficiency of iteration.²³ After determining photo- z 's for this subsample, we compute the median ratio between the best-fit template fluxes and the catalog fluxes in each photometric band. We then rerun EAZY, correcting the flux through each band by multiplying the flux by this ratio. We iterate this process until the flux ratios converge within 1% of unity (as in Ilbert et al. 2006). The *XMM*-LSS is nearly uniformly covered by the SERVS survey (modulo a tiling pattern) but features three separate levels of depth in the optical from the HSC. Differences in coverage and depth affect the relative weight of given bands in the fit and therefore may affect the zero-point corrections. We therefore

perform this procedure separately for the HSC Wide, Deep, and Ultradeep patches. The zero-point magnitude offsets computed in this way are presented in Table 1. We note that these offsets are correcting for the fact that the particular template set used by EAZY may not be fully representative of the real galaxies spectra, as well as for any systematic offsets in the photometry.

After the above procedure, the bulk of the sources ($>96\%$) show nominally excellent fits with reduced $\chi^2 < 3$. The $p(z)$ are typically single peaked but show increasing incidences of multiple peaks with increasing K_s magnitude. By adopting a $K_s < 23$ cut as discussed above, we minimize the effect of multiple significant solutions. In addition, in the density map analysis presented in the next section, the full $p(z)$ profiles for each galaxy are taken into account, and therefore any remaining sources with multiple peaks naturally have lower weight in the density map calculation.

Our choice of using a template-based method for deriving photometric redshifts is driven by the fact that non-template-based methods rely more heavily on training on the spectroscopic sample. This requires a spectroscopic sample that is representative of the whole. The left panel of Figure 2 shows the optical color-magnitude diagram comparing the full photometric catalog with the subset of galaxies with spectroscopic redshifts. It is clear that the spectroscopic subset is not representative of the whole. This is further highlighted in the right panel of Figure 2, where we show the photometric redshift

²³ We tested using a random subsample of galaxies in our sample to avoid using the biased spectroscopic subsample. We found no significant differences in the resulting redshift distribution.

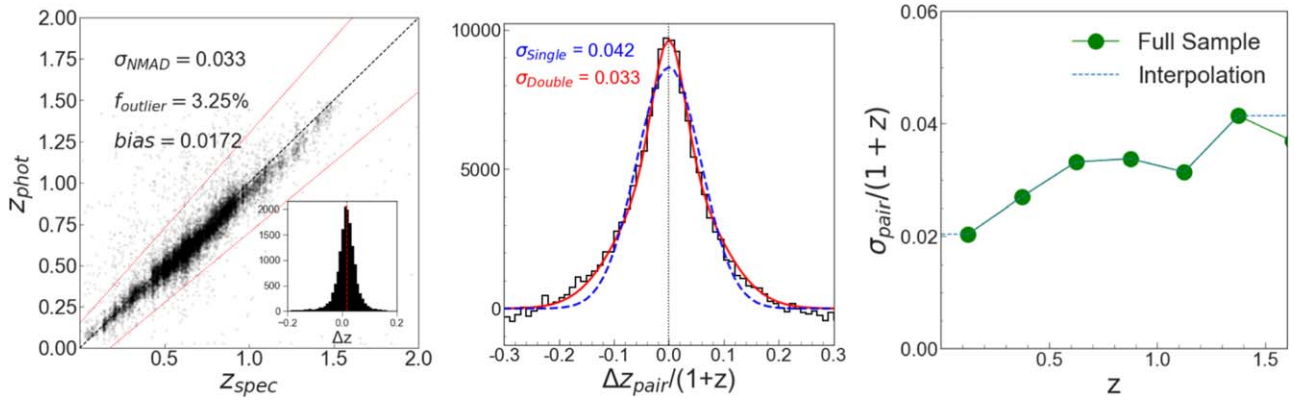


Figure 3. Left: comparison of photo- z with quality spec- z for galaxies with $z_{\text{phot}} < 1.5$. The inset shows the distribution of Δz_{pair} from which we derive σ_{NMAD} after removing the outliers. Points that do not lie between the dotted red lines are considered outliers. Middle: photo- z uncertainty distribution for sources with $z_{\text{phot}} < 1.5$ based on the pair analysis. The single (blue) and double (red) Gaussian fits are overlaid. The double Gaussian is clearly a better fit to the distribution and provides a weighted $\sigma_{\text{pair}}/(1+z) = 0.033$. Right: evolution of photo- z uncertainty from $0.0 < z < 1.6$. The blue dashed line is an interpolation of the function as described in 3.2.1.

distribution of all our sources compared with the spectroscopic redshift distribution. It is clear that at redshifts of $z \gtrsim 1$, methods that heavily rely on spectroscopic redshift training will start to fail/be less reliable. We have not explored the validity of the observed peak in the redshift distribution at $z \sim 1.9$, but our analysis does not extend that far; therefore, we ignore it at this point.

3.1.1. Photometric Redshift Accuracy

We assess the photo- z accuracy in two ways (Figure 3). We begin with the standard approach of comparing the photometric and spectroscopic redshifts. We characterize the accuracy of the photo- z 's via

$$\sigma_{\text{NMAD}} = 1.48 \times \text{median} \frac{|z_{\text{spec}} - z_{\text{phot}}|}{1 + z_{\text{spec}}}, \quad (1)$$

where σ_{NMAD} (the normalized median absolute deviation) is robust against catastrophic photo- z failure. We identify outliers as objects with $|z_{\text{spec}} - z_{\text{phot}}| > 0.15$ (as in Dahlen et al. 2013; Ilbert et al. 2013). Before computing σ_{NMAD} , we remove outliers from the distribution. This helps characterize the distribution of only those sources that had relatively successful photo- z fits. We calculate $\sigma_{\text{NMAD}} = 0.033$ for our field, with outlier fraction $f_{\text{outlier}} = 3.25\%$ and a bias of 0.0172. We correct for this bias when we compute our density maps.

However, this standard approach has the drawback that the subsample with spectroscopic redshifts is not representative of the sample as a whole in a color-magnitude diagram (Figure 2). To overcome this, we also characterize our uncertainty using the pair method of Quadri & Williams (2010). This method does not give reliable outlier fractions or bias estimates but uses the full photometric sample to compute $\sigma_z/(1+z)$. This gives us sufficiently large numbers, especially above $z \sim 1$, to allow us to assess the uncertainties as a function of redshift.

The pair method exploits the observation that galaxies with close angular separation have a significant probability of being physically associated, while the role of line-of-sight projections can be subtracted in a statistical sense. It works as follows. For each galaxy in our sample, we first search for pairs separated by $2''.5$ – $15''$. Galaxies often contain multiple pairs in this annulus, so the following procedure is done for all such pairs. For each

pair we compute

$$\Delta z_{\text{pair}} = (z_{\text{phot},1} - z_{\text{phot},2})/(1 + z_{\text{mean}}), \quad (2)$$

where z_{mean} represents the mean redshift of the pair. We then randomly assign each object new coordinates in the field and perform the same procedure to obtain the distribution of Δz_{pair} for random line-of-sight projections. Subtracting the random distribution of Δz_{pair} from the observed distribution of Δz_{pair} gives the distribution for physically associated galaxy pairs only.²⁴ This distribution for our full sample of $z < 1.5$ galaxies is shown in the middle panel of Figure 3. The width of this distribution is a factor of $\sqrt{2}$ larger than the photo- z uncertainty per galaxy (because we are dealing with pairs of galaxies).

In the middle panel of Figure 3, we show that a single Gaussian can be a poor fit owing to the presence of extended wings on either side of the peak. As discussed in Quadri & Williams (2010), these wings likely result from the nonflat redshift distribution of our field. We follow the recommendation of Quadri & Williams (2010) and fit the distribution by a convolution of two Gaussians (see Quadri & Williams 2010, for full details) centered about zero. The weighted sum of the standard deviations of the two Gaussians gives $\sigma_{\text{pair}}/(1+z)$ using this method. For our sample, this double Gaussian is clearly the better fit and gives an uncertainty $\sigma_{\text{pair}}/(1+z) = 0.033$, consistent with σ_{NMAD} derived above.

The right panel of Figure 3 shows the thus-derived uncertainty as a function of redshift, in bins of $\Delta z = 0.25$. We find that the uncertainties $\sigma_{\text{pair}}/(1+z)$ get significantly worse at $z \gtrsim 1.5$; therefore, for the density map analysis in the following sections, we will restrict ourselves to $0.1 < z < 1.5$.

3.2. Surface Density Maps: Method and Validation

We follow the method of Darvish et al. (2015b), who construct 2D density maps based on photometric (and, where available, spectroscopic) redshifts in the COSMOS field. In this method the surface density is estimated in redshift slices via weighted adaptive kernel smoothing. This means that the kernel width adapts to the local density as described below. This method allows us to probe adaptively smaller volumes than the more commonly

²⁴ The characteristic velocity differences between such physical pairs are much smaller than the photometric redshift uncertainties. Therefore, we ignore this effect.

Table 2
Redshift Slices and Comoving Depths

Bin	z-range	Depth (Mpc)	Bin	z-range	Depth (Mpc)
1	$0.1 < z < 0.146$	192	15	$0.549 < z < 0.649$	317
2	$0.123 < z < 0.171$	197	16	$0.599 < z < 0.705$	324
3	$0.146 < z < 0.196$	203	17	$0.649 < z < 0.760$	330
4	$0.171 < z < 0.224$	210	18	$0.705 < z < 0.820$	330
5	$0.196 < z < 0.251$	217	19	$0.760 < z < 0.879$	330
6	$0.224 < z < 0.282$	227	20	$0.820 < z < 0.942$	325
7	$0.251 < z < 0.313$	237	21	$0.879 < z < 1.004$	322
8	$0.282 < z < 0.348$	246	22	$0.942 < z < 1.069$	315
9	$0.313 < z < 0.382$	254	23	$1.004 < z < 1.133$	309
10	$0.348 < z < 0.421$	265	24	$1.069 < z < 1.207$	318
11	$0.382 < z < 0.460$	275	25	$1.133 < z < 1.281$	327
12	$0.421 < z < 0.504$	287	26	$1.207 < z < 1.372$	347
13	$0.460 < z < 0.549$	298	27	$1.281 < z < 1.462$	365
14	$0.504 < z < 0.599$	308	28	$1.372 < z < 1.564$	368

used fixed-aperture “cylinders.” The weights account for photometric redshift uncertainties, which helps combat the significant smearing of the signal along the line of sight (see Muldrew et al. 2012, for a comparison between different density estimation methods).

3.2.1. Redshift Slices

To obtain our redshift slices, we first linearly interpolate the redshift evolution of $\sigma_{\text{pair}}/(1+z)$ onto a finer grid. Starting with $z = 0.1$, we set the start and end points for our bins such that each slice width is $2 \times \sigma_{\text{pair}}$ evaluated using the interpolation shown in the right panel of Figure 3. We use overlapping redshift slices so that if a given overdensity falls on the edge in one slice and therefore is significantly scattered outside of the slice, it will, by design, end up in the middle of the neighboring overlapping slice. Our redshift slices and their comoving depths are given in Table 2.

3.2.2. Weighted Adaptive Kernel Smoothing

The weighted adaptive kernel smoothing works as follows. For each redshift slice, we identify the objects whose median photo- z falls within that slice. We then weight each of the galaxies within our redshift slice by the fraction of that object’s total $p(z)$ that lies within the slice of interest. We proceed to estimate the surface density $\hat{\Sigma}(\mathbf{r}_i)$ at each object’s location by summing over a kernel K . In Darvish et al. (2015a) this kernel is a weighted 2D Gaussian whose width starts at $h = 0.5$ Mpc but is adaptive, i.e., scaled by the local density in a manner analogous to that described below. We test this algorithm first by taking the public COSMOS data and reproducing the density map around a filament at $z \sim 0.5$ that was published in Darvish et al. (2015b). While we successfully reproduce the results of that study, we find the code to be slow.²⁵ We test three faster alternatives: a truncated Gaussian kernel $K_G(h)$, an Epanechnikov (parabolic) kernel $K_E(h)$, and a top-hat kernel $K_T(h)$. The Epanechnikov kernel is defined as

$$K_E(\mathbf{r}_i, \mathbf{r}_j, h) = \begin{cases} \frac{3}{4h^2} \left(1 - \left(\frac{\mathbf{r}_i - \mathbf{r}_j}{h}\right)^2\right) & \text{where } |\mathbf{r}_i - \mathbf{r}_j| < h \\ 0 & \text{else,} \end{cases} \quad (3)$$

²⁵ We ran timing tests and found the full Gaussian kernel to be $25 \times$ slower for a test run of $\approx 10^3$ objects compared to the alternatives listed, which all took comparable time.

where \mathbf{r}_i is the position of the object and \mathbf{r}_j is the position of each other object.

Following Darvish et al. (2015a), we choose an initial fixed kernel width h for the Gaussian kernel of 0.5 Mpc, which corresponds roughly to R_{200} for a halo of $10^{13} M_\odot$. For the Epanechnikov kernel we get equivalent results using an initial value of $h = 1.0$ Mpc. Using a fixed width would underestimate the density in overdense regions and overestimate the density in underdense regions, so we calculate an adaptive smoothing width $h_i = h \times \lambda_i$ for each object. Here $\lambda_i = \sqrt{G/\hat{\Sigma}(\mathbf{r}_i)}$, where G is the geometric mean of all $\hat{\Sigma}(\mathbf{r}_i)$ values. To compute the surface density in our redshift bins, we set up a regular grid in steps of 50 kpc. Thus, 50 kpc sets the minimum scale probed by our maps in the plane of the sky. On top of this grid, the density maps are computed using the same kernel, but now using the adaptive width h_i . This surface density is converted to an overdensity with respect to the median surface density Σ_m in the slice as follows:

$$\delta = \frac{\Sigma - \Sigma_m}{\Sigma_m}. \quad (4)$$

To help us decide between the different kernel options, we compute density maps using exact redshifts from the simulated light cone and the bins defined in Table 2. In Figure 4 (top panels) we show the relation between the percentage rank of measured 2D overdensities and dark matter halo mass (using the main host halo mass for each galaxy in our simulated light cone, not subhalos) for all galaxies in the range $0 < z < 1$. For all kernels, we find that the most overdense regions tend to correlate with high halo masses, suggesting that we can indeed recover the peaks of the density field with this method. To further help us differentiate between them, we consider two measures. The first tells us how often a significant overdensity is observed when there is no corresponding high-mass halo (i.e., a false-positive measure). We compute this as the fraction of galaxies found in >80 th percentile overdensities that are located in halos with $\log(M_{\text{halo}}/M_\odot) < 12(f_{\text{lowmass}})$. The other important measure is how closely halo mass maps onto overdensity percentile (i.e., an accuracy measure). We compute this as the width of the halo mass distribution for all galaxies found in 80th percentile overdensities after removing the galaxies in halos with $\log(M_{\text{halo}}/M_\odot) < 12(\Delta_{\text{highmass}})$. The Epanechnikov filter performs the best in both measures, although the differences between the three filters are fairly minor. In the bottom panels of Figure 4, we do the same analysis for galaxies in the range $1 < z < 1.5$. We find that the basic trends hold, although, as expected, the false-positive rate is now higher. This, however, is the result of using a fixed percentile (here 80%) in selecting significant overdensities. As discussed below, we find that it is more appropriate to use an evolving percentile threshold.

3.2.3. Probing the Density Field with Photometric Redshifts

Here we investigate the recoverability of true overdensities given the uncertainties in our photometric redshifts. We choose an arbitrary 4.8 deg^2 subsection of the simulation to match the area of our XMM-LSS field and perform the density map analysis using both the exact redshifts and redshifts minimizing the photometric redshifts (see Figure 5). To mimic what we do with the observed data, where we use the $p(z)$ output from EAZY for each galaxy, we assign an uncertain “photometric”

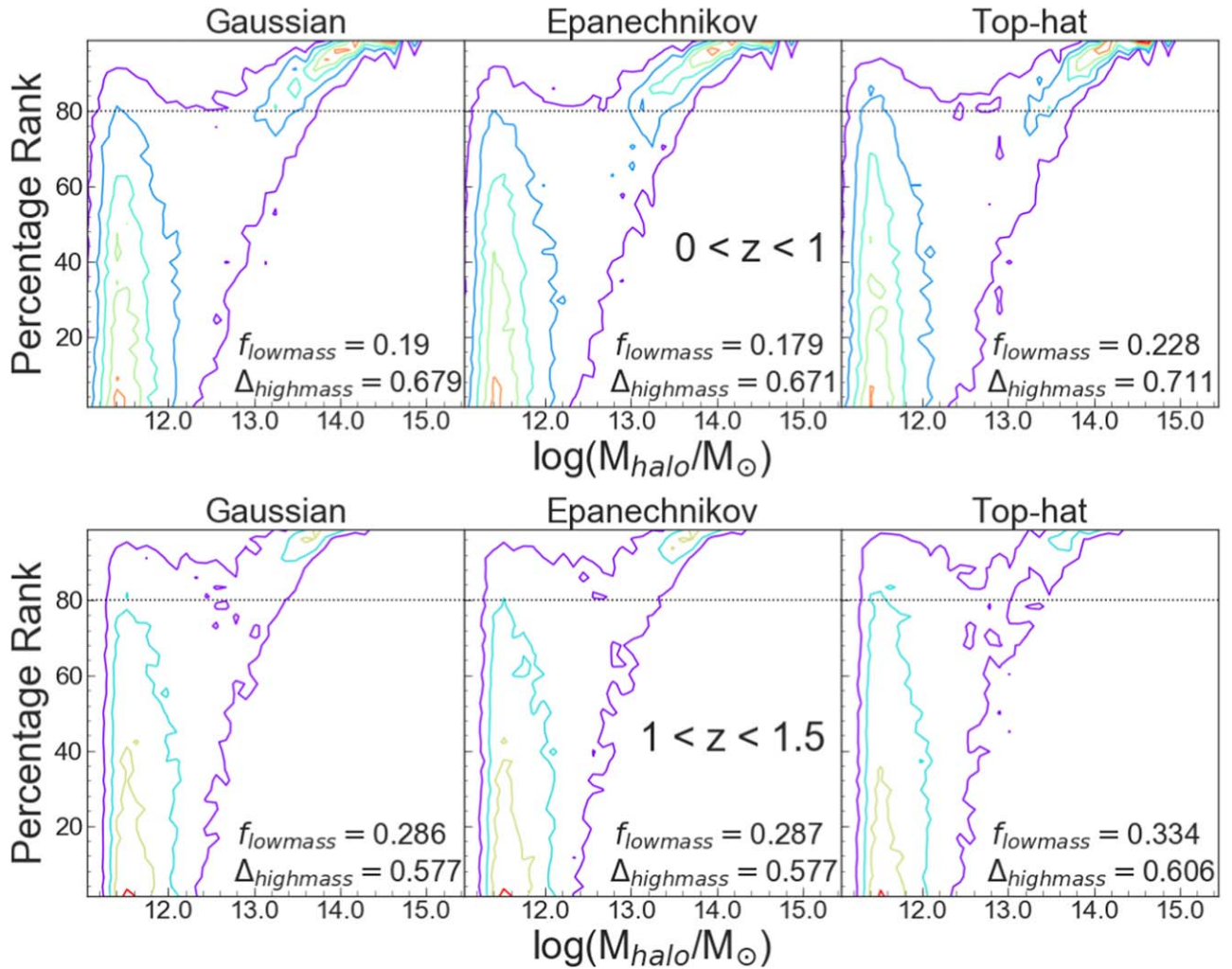


Figure 4. Here we use the 2D density maps calculated using the exact redshifts of the simulated galaxies to show how the overdensity percentile compares with the host halo mass associated with each simulated galaxy. The top panels use all galaxies in the range $0 < z < 1$, and the bottom panels use all galaxies in the range $1 < z < 1.5$. Contours are linearly spaced and indicate constant galaxy number. These show that the bulk of galaxies that reside in high (>80th) percentile overdensities live in high-mass halos ($\log(M_{\text{halo}}/M_{\odot}) > 13$, which is roughly group scale). Therefore, finding high percentile overdensities helps us find high-mass halos. We compare this behavior using a truncated Gaussian filter (left), an Epanechnikov kernel (middle), and a top-hat kernel (right). Here f_{lowmass} is the fraction of galaxies above the 80th percentile within $\log(M_{\text{halo}}/M_{\odot}) < 12$, while Δ_{highmass} is the width of the distribution of galaxies above the 80th percentile. On both counts, the Epanechnikov filter performs marginally better than the truncated Gaussian, while the top-hat filter is the worst performing.

redshift to each galaxy by drawing from a Gaussian distribution centered on the galaxy’s exact simulated redshift z_{exact} and a width given by the typical width of a galaxy’s $p(z)$.²⁶ We note that this is wider than $\sigma_{\text{pair}}(z)$ since this incorporates outliers, multiple- z solutions, etc. We use this wider width, as it approximates better what we can do with the data themselves. We know that this works since we get reasonably close distributions of $\log(1 + \delta)$ between simulations and data in this way. For a random subset of 3.25% of the objects, we assign a redshift drawn from a uniform distribution in the range $0 < z < 3$ to mimic the catastrophic outlier fraction. Lastly, 3.7% of the objects are given redshifts equal to their exact simulated redshift to mimic our spec- z fraction. The latter fraction, of course, is a function of redshift. However, it is small enough that its role is negligible here.

Figure 5 shows an arbitrarily chosen redshift slice at $0.649 < z < 0.760$, where we compare the surface density

computed using the exact redshifts versus uncertain redshifts as determined above. This figure highlights that the main large-scale structures and strongest overdensities are largely preserved. This means that we are likely to recover features, real or projected, that would appear if we had exact redshifts given the slice width we are using. There are, however, significant differences as well. The amplitudes of the overdensities are generally lower in the uncertain redshift map (as expected). This is because the uncertainty in the redshifts tends to “smear” the signal and decrease the magnitude of over- and underdensities. Also apparent are some weaker “false” features in the uncertain redshifts map not present in the exact map (see e.g., upper right end of the maps). These arise owing to real overdensities that belong to neighboring redshift slices being scattered into this slice by redshift uncertainties.

Next, we investigate how reliably 2D density maps calculated including redshift uncertainties track the mass of the host halo of the galaxies in the simulated light cone. The left panel of Figure 6 is similar to Figure 4 in that it plots the percentile of the overdensity in which a galaxy is found against

²⁶ We do not specifically simulate double-peaked distributions, as these form a negligible fraction of the whole for our $K < 23$ sample.

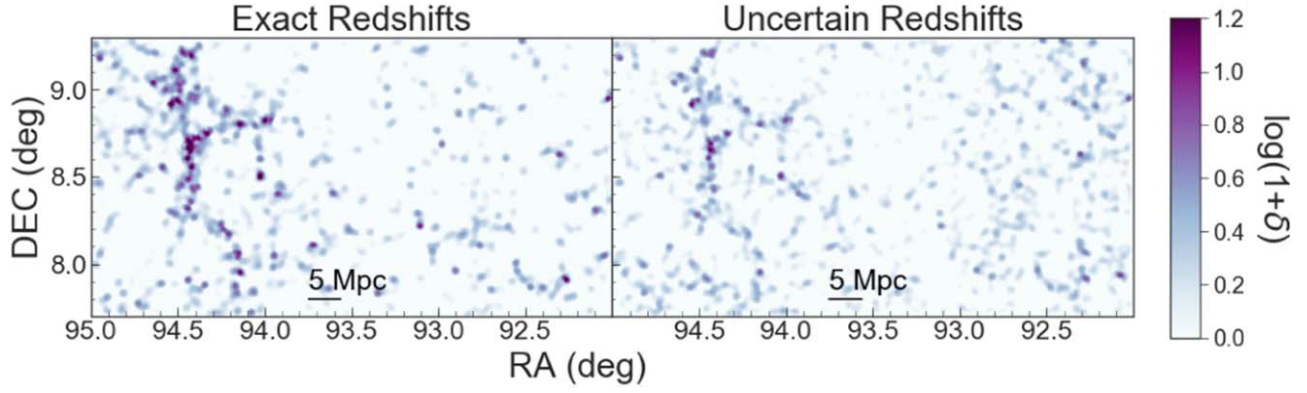


Figure 5. Smoothed density maps of our simulation over the range $0.649 < z < 0.760$ using the Epanechnikov kernel. Left: density map using exact redshifts. Right: density map using uncertain redshifts mimicking our photometric redshift errors as described in text. These show that while the high-density peaks are weaker in the uncertain redshifts map, overall both the peaks and the large-scale structure are preserved.

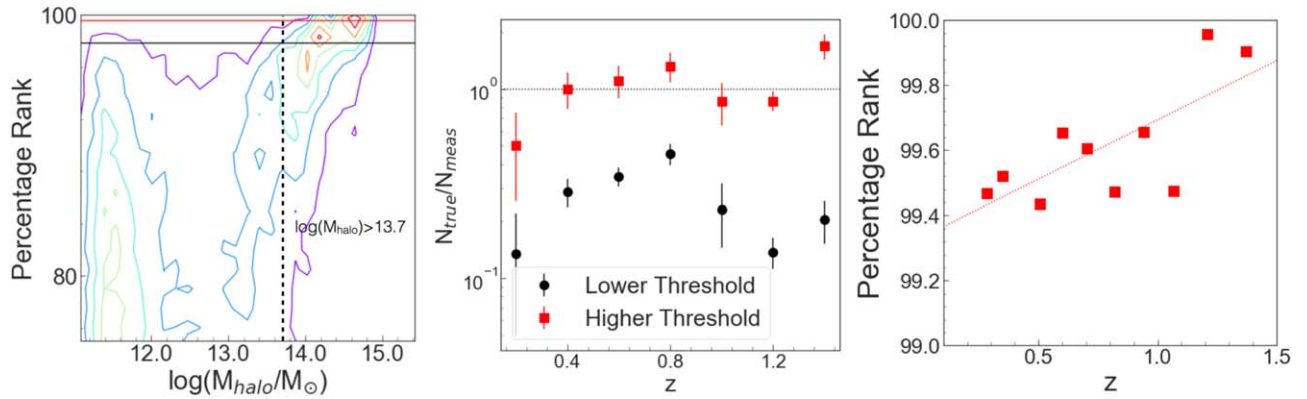


Figure 6. Left: similar to Figure 4, but now including the uncertainty in the photometric redshifts. This has the effect of scattering galaxies from low-density environments to high-density ones and vice versa. The group scale is no longer reliably recovered, as many galaxies in smaller mass halos are found in $>80\%$ overdensities. If we consider the recoverability of cluster scales (here defined as $M_{\text{halo}} > 10^{13.7} M_{\odot}$), however, they can still be recovered at higher percentile levels. The red and black horizontal lines are two test recoverability percentiles. Middle: recoverability of $\log(M_{\text{halo}}/M_{\odot}) > 13.7$ using these two test thresholds as evaluated by $N_{\text{true}}/N_{\text{measured}}$ (see text for details). The dotted black line corresponds to $N_{\text{true}}/N_{\text{measured}} = 1$, which corresponds to a minimal false-positive rate—the higher red threshold is therefore preferable by this measure. Right: median percentage ranks to recover $\log(M_{\text{halo}}/M_{\odot}) > 13.7$ as a function of redshift. Note that this threshold increases with redshift as expected from hierarchical halo growth.

its host halo mass. However, here the density maps are computed using uncertain redshifts (mimicking our photometric redshift errors). We again see a bimodality in this distribution about a group scale ($\log(M_{\text{halo}}/M_{\odot}) \sim 13$), above which halo mass correlates with observed 2D overdensity. However, there are two marked differences: (1) there is significant presence of lower-mass halos in high-density parts of the maps, and (2) there is significant range in observed percentile per halo mass. Given the first point, we can only reliably recover halos with $\log(M_{\text{halo}}/M_{\odot}) \gtrsim 13.7$ going to higher percentiles in the density maps.

How reliably can we recover clusters (here defined as $\log(M_{\text{halo}}/M_{\odot}) > 13.7$)? Given the second point above, we need to find what percentile threshold mass for finding halos above said scale minimizes false positives and false negatives. The middle panel of Figure 6 illustrates this further by considering two different test thresholds aimed at finding halos with $\log(M_{\text{halo}}/M_{\odot}) > 13.7$. Here we measure $N_{\text{true}}/N_{\text{measured}}$, the ratio of all halos in the simulation that meet the mass criteria to all such halos that are recovered using the particular percentile threshold. This ratio ideally should be ≈ 1 , with a value $\ll 1$ showing a significant number of false positives (suggesting that the percentile threshold is too low) and a value

$\gg 1$ showing a significant number of false negatives (suggesting that the percentile threshold is too high).

In the right panel of Figure 6 we show the percentile threshold that recovers $\log(M_{\text{halo}}/M_{\odot}) > 13.7$ with $N_{\text{true}}/N_{\text{measured}} \approx 1$ as a function of redshift. This threshold increases with redshift as expected from hierarchical halo mass growth—i.e., a high-mass halo is more of an extreme in the density field at higher redshift than at lower redshift. This evolving threshold is given by

$$\text{Percentile}_{13.7} = 0.355z + 99.4. \quad (5)$$

3.3. Observed *SERVS* XMM-LSS Density Maps

To compute the surface density maps for our observed data in the XMM-LSS field, we first correct for the measured bias in the photometric redshifts by multiplying the redshifts by 1.0172. We also generate a mask where bright stars (based on the bright star mask of Mauduit et al. 2012), the field border, and image artifacts are all masked. This mask brings the usable area of the field down to 4.0 deg^2 . For consistency, we mask a 0.8 deg^2 area out of the border of the simulated field. This matches the area but obviously not the exact geometry of the observed masked field—this is not relevant to the present paper but needs to be considered for any large-scale structure studies.

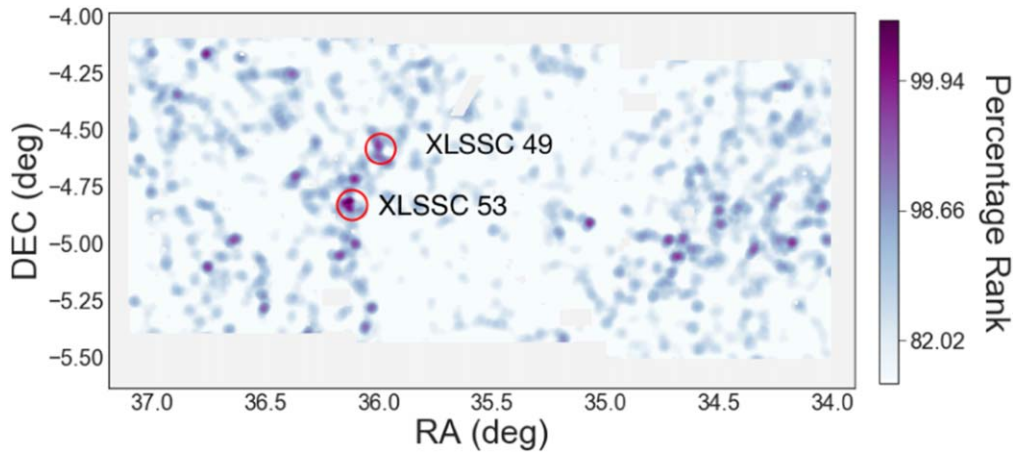


Figure 7. Sample *XMM*-LSS density map at $0.421 < z < 0.504$. The red circles mark two known spectroscopically confirmed X-ray clusters (Clerc et al. 2014), XLSSC 49 and 53, both of which are located at $z = 0.50$.

In addition, there is some nonuniformity of coverage across the field, in particular with about 1/3 being covered by the deeper optical HSC-Ultradeep patch and the rest being covered by HSC-Deep. The difference in depth in the *grizy* bands leads to lower uncertainties in the photometric redshifts for the HSC-Ultradeep patch than in the HSC-Deep patch. This means that they suffer less smearing, and we end up seeing higher overdensities of sources in this patch, especially at $z \gtrsim 1$. We found that this nonuniformity is minimized by using percentiles rather than the measured overdensities in determining thresholds for finding significant overdensities (which is why we used percentiles in finding the threshold for selecting $\log(M_{\text{halo}}/M_{\odot}) > 13.7$ halos in Section 3.2.3).

Figure 7 gives an example of a density map for the *XMM*-LSS field. It shows qualitatively similar behavior to that of the simulated maps shown in Figure 5. In particular, we see very similar large-scale filamentary structures. We defer our analysis of such structures to a subsequent paper in this series. We also circle two previously known spectroscopically confirmed X-ray clusters, both recovered by our density maps (Overdensities 69 and 92 in Table 3; see Section 3.4 for details).

3.4. Potential New Clusters in *XMM*-LSS

Using our density maps for *XMM*-LSS and the percentile threshold for recovering halos of $\log(M_{\text{halo}}/M_{\odot}) > 13.7$ given in Equation (5), we find 330 potential halos with $\log(M/M_{\odot}) > 13.7$ in the range $0.1 < z < 1.5$ (339 if we allow for a few more clusters that may be in this range or in the slice just above). Due to the use of overlapping redshift slices, overdensities found in neighboring slices in overlapping R.A.–decl. locations are counted only once. They are assigned to the slice in which they are strongest. Our overdensities are listed along with their basic characteristics in Table 3. Note that for overdensities selected in more than one slice the redshift ranges given in the table conservatively span both slices.

The redshift distribution of our overdensities is given in the left panel of Figure 8, where overdensities spanning more than one redshift slice (see above) are assigned to the one where they have the highest percentile. We overlay on that the redshift distribution of all halos with $\log(M_{\text{halo}}/M_{\odot}) > 13.7$ expected in our field based on our simulated light cone. We expect 279 ± 35 such halos in the *XMM*-LSS. This error bar represents the spread in this number when drawing random 4 deg^2 patches from our

18 deg^2 simulated light cone and therefore approximates cosmic variance.²⁷ We note that, at nearly 13%, cosmic variance is significant at this mass scale even for our relatively large field. In the same figure we overlay the histogram derived by applying photometric redshift uncertainties to our light cone, generating 2D density maps and extracting likely clusters based on the exact same procedure as applied to the real data. The fact that this distribution recovers quite closely the simulated halo histogram suggests that our procedure is robust in recovering such structures.²⁸ The recovered such structures from the observed *XMM*-LSS field are also quite close—indeed, it is only $\approx 18\%$ above the expected number from the simulated light cone (only a few percent above if we take the upper limit from our cosmic variance test). This difference is small enough that it can still be attributed to cosmic variance (given our rough estimate thereof). However, it can also be due to a nonnegligible false-positive rate. This could result from slightly overestimating our redshift uncertainties—which means that we have less redshift smearing and somewhat higher densities than in the simulations.

In Table 3 we also include a morphology column that flags overdensities that have significant spatial extent. This is computed by making 80×80 pixel cutouts around each overdensity and computing the fraction of that patch that is above our density threshold. By visual inspection we chose $>10\%$ as signifying extended overdensities. About 1/4 of our overdensities fall in this category. These are likely to be dominated by projection effects given the wide redshift slices, as well as the effects of large-scale structure such as clusters apparently embedded in filaments as shown in Figure 7. These can also include cases of cluster mergers as discussed in Section 3.4.2.

3.4.1. Confirming Previously Known X-Ray Clusters

In Table 3 we also note which of our overdensities are previously known in the literature. For this comparison we looked at the XLSSC catalog of Adami et al. (2018). Within our field and above $z = 0.1$, there are 70 X-ray clusters that are

²⁷ This is only a rough approximation since in our light cone we have <5 independent realizations.

²⁸ Since we ultimately derive our percentile threshold on the same simulations, this is not surprising but a good sanity check. Of course, we also assume that the simulated light cone itself is a good representation of reality, which previous studies suggest is the case (e.g., Lagos et al. 2012).

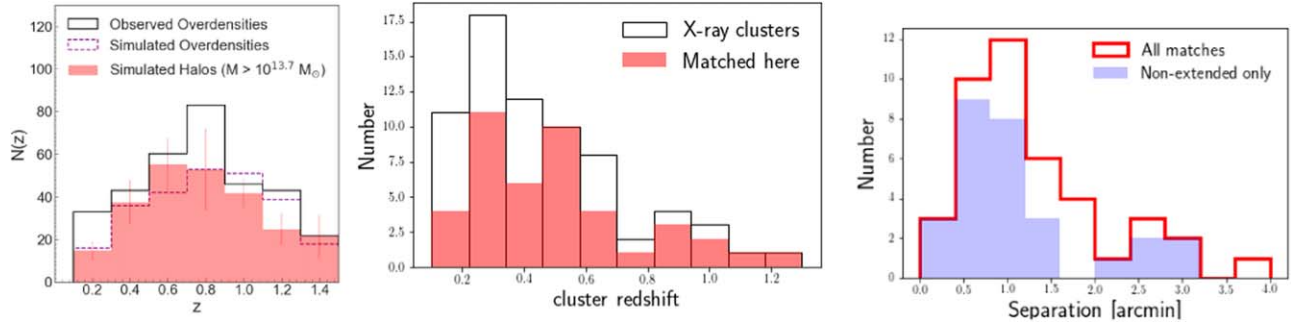


Figure 8. Left: histogram of overdensities corresponding to $M_{\text{halo}} \gtrsim 10^{13.7}$ within an area of 4.0 deg^2 . The solid black line shows the distinct overdense regions above the threshold in our sample. In purple are the distinct overdense regions above the threshold in the simulated light cone with degraded redshift accuracy. For reference, in red is the distribution of halos with $M_{\text{halo}} \gtrsim 10^{13.7}$ in the simulation in our sample as a function of redshift. The height of the red histogram is found by dividing the 18 deg^2 of the light cone into four quadrants and averaging the count of halos in each quadrant (scaled by $4.0/4.5$). The error bars represent the maximum and minimum count among the four quadrants to give some sense of the impact of cosmic variance. Middle: the open histogram represents the spectroscopically confirmed X-ray clusters in the field based on Adami et al. (2018), where the minimum cluster mass is $\log(M_{500}/M_{\odot}) = 13.3$, which is below our target halo mass. The X-ray selection leads to increasing mass limit with increasing redshift. The filled histogram represents the known X-ray clusters we recover from our density maps. The relative dearth of recovered clusters at lower redshifts is the result of the lower cluster masses thereof. Right: separations between the positions of our overdensities and their closest-matching X-ray clusters. Note that at $z \sim 0.2-1$, $1''$ corresponds to $\approx 200-500 \text{ kpc}$. The shaded histogram shows this distribution for the nonextended overdensities only. It is clear that these separations are largely driven by the uncertainty in the center positions of the overdensities.

Table 3
Overdensities Selected in the XMM-LSS Field

ID	R.A.	Decl.	$z\text{-range}^a$	N_{spec}^b	Morphology	References ^c
1	36.7988	-5.0698	0.100-0.196	3
2	36.3951	-4.2480	0.100-0.196	13	...	XLSSC41.0, $z = 0.142$ [C14, A18]
3	34.0523	-4.2236	0.100-0.196	3	...	XLSSC57.0, $z = 0.153$ [C14, A18]
4	36.4396	-4.3284	0.123-0.223	18	Extended	...
5	35.3947	-4.5792	0.146-0.251	2	Extended	XLSSC119.0, $z = 0.158$ [A18]
6	35.5526	-4.2187	0.146-0.251	2
7	35.0743	-4.6531	0.146-0.251	3
8	34.8840	-4.5052	0.146-0.251	6
9	36.4270	-4.9823	0.171-0.282	2
10	35.4948	-4.4999	0.171-0.282	0	Extended	...
...	35.4948	-4.4999	0.171-0.282	0	Extended	...

Notes.

^a The full redshift range within which overdensity is found.

^b These are the only high-quality spectroscopic redshifts within a circle of 750 kpc (proper) of the overdensity center.

^c References are as follows: A18—Adami et al. (2018); C14—Clerc et al. (2014); B06—Bremer et al. (2006); vB07—van Breukelen et al. (2007).

(This table is available in its entirety in machine-readable form.)

spectroscopically confirmed from this catalog. We matched these against our overdensities using a $0''.07$ separation (corresponding to $\approx 1.5 \text{ Mpc}$ at $z \sim 0.5$). We also excluded potential matches whose cluster redshift was outside the redshift range of our overdensities (with a small padding since clusters just outside our redshift slices would likely influence the density map through the scatter of their photometric redshifts). There were 53 such matches in Table 3; however, several known clusters were matches to more than one of our overdensities owing to the generous redshift slices. All cases where a matched cluster was just outside the overdensity redshift slice also had the same cluster matched to another overdensity where it is inside the redshift slice. We chose to keep these double matches since, as described above, massive clusters would influence neighboring slices owing to photometric redshift scatter.

Altogether there were 43 matches to unique known clusters. These represent 61% of the X-ray clusters in the field. As shown in the right panel of Figure 8, most of the unmatched clusters are at lower redshifts ($z < 0.5$), consistent with the expected lower

halo masses therein (the XLSSC catalog of Adami et al. 2018 has a limiting cluster mass of $\log(M_{\text{halo}}/M_{\odot}) > 13.3$, below our halo mass threshold, but this threshold increases with redshift, consistent with the increased recoverability in our density maps. For example, for the smaller subset of X-ray clusters in Clerc et al. (2014) (which are all folded into the XLSSC catalog), we recovered 17/21 in our density maps but found that the “missing” four clusters were all associated with density percentiles $> 88\%$ —i.e., still significant but below our threshold for finding halos of $\log(M_{\text{halo}}/M_{\odot}) > 13.7$. The clusters that are also in Clerc et al. (2014) are marked in Table 3. In addition, our Overdensity #282 corresponds to XLSS J022303.0043622 at $z \sim 1.22$ first found by Bremer et al. (2006). Lastly, van Breukelen et al. (2007) found a spectroscopic cluster at $z = 1.454$ associated with our Overdensity #311 (more on this structure below).

3.4.2. Case Studies

Detailed discussion of the clusters and large-scale structures is reserved for a subsequent paper in this series. However, as an illustration of the potential of our technique to find distant

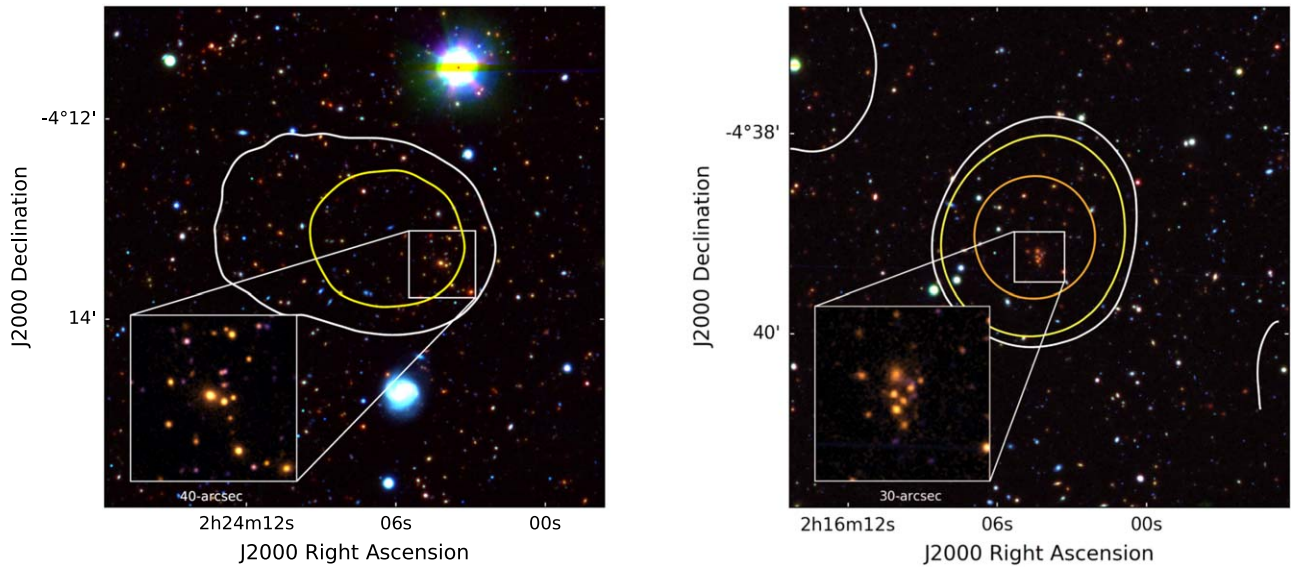


Figure 9. Two distant galaxy clusters corresponding to overdensities in the *XMM*-LSS field. Left: field of the $z = 1.05$ X-ray-detected cluster XLSSC 029 of Clerc et al. (2014), with contours of overdensity 0.6 in white and 0.8 in yellow. Right: highest overdensity in the $1.372 < z < 1.564$ redshift bin, with contours of overdensity as follows: 0.25 in white, 0.5 in yellow, and 1.0 in orange. In both cases, the red channel of the RGB image is *Spitzer* IRAC $4.5 \mu\text{m}$, the green channel the VIDEO *H* band, and the blue channel the HSC ultra-deep *i* band. The insets show zoom-ins of the compact cluster cores, with VIDEO K_s data in red, VIDEO *H*-band data in green, and HSC ultra-deep *i*-band data in blue.

clusters, in Figure 9 we show the overdensity corresponding to the highest-redshift X-ray-detected cluster in the field from Clerc et al. (2014), XLSSC 029 at $z = 1.05$, and an example of what appears to be a compact cluster core associated with the highest percentile overdensity in our highest-redshift bin ($1.372 < z < 1.564$, Overdensity #336).

As discussed in Section 3.4, a quarter of our overdensities show extended morphologies that are likely the result of projection effects—i.e., 3D structures that are unassociated but overlap on the sky, but they can also include interesting potentially associated structures such as cluster mergers. We examine one of our extended sources in more detail, Overdensity #300, which is chosen because it is among our higher-redshift structures but also has significant spectroscopic redshift coverage. It gives us an example of how, by looking at the structures in overlapping redshift slices, we get a coarse view of the 3D structure.

Examining this overdensity more closely reveals a potential cluster merger at $z = 1.28$. This is shown in Figures 10 and 11. In Figure 10 we show this structure in three overlapping redshift slices shown on either side. The field had been previously noted as overdense by van Breukelen et al. (2007), who obtained spectroscopy of galaxies in the field with the Keck Telescope. We find that the bipolar overdensity structure in our maps corresponds to a peak in the distribution of spectroscopic redshifts at $z \sim 1.28$ (bottom left), and Figure 11 shows that the distribution of objects at this redshift on the sky corresponds well to the overdensity map. The relative line-of-sight velocity (relative to the median in this peak) is shown on an R.A.–decl. plot highlighting the gradient across this structure. Component A has a median spectroscopic redshift of 1.286 with a velocity dispersion of 670 km s^{-1} . Component B has a median redshift of 1.276 with a velocity dispersion of $\sim 1100 \text{ km s}^{-1}$ (likely affected by the overlapping structure at lower redshift clearly visible in the lower-redshift slice). Even

without correcting for this structure in its median redshift (since we cannot cleanly disentangle these structures), the relative velocity between these two components is 3000 km s^{-1} . To check whether this number is reasonable for a potential cluster merger, we compared it with the relative velocity of the “bullet” and the larger cluster in the well-studied Bullet Cluster. This is estimated at 2700 km s^{-1} (Springel & Farrar 2007). This is the true relative velocity rather than the line-of-sight one as in our case, but it does show that our number is of reasonable magnitude, especially considering that the median redshift of Component B is likely pulled down by the slightly foreground structure.

Figure 10 also helps illustrate how structures at slightly higher and lower redshifts “bleed” into any given redshift slice, but the overlapping slices help us discern some of the 3D structure. For example, Overdensity #311 sits on top of Components A and B in the middle maps. It is, however, increasingly stronger in the two overlapping density slices centered at higher redshifts, suggesting that what we see here is coming in from a strong overdensity that is actually more distant. Indeed, van Breukelen et al. (2007) find six objects in the field at $z \approx 1.45$, confirming that Overdensity #311 is background to our potential merger.

This particular structure is chosen owing to the quality of spectroscopic coverage, which makes it more likely to be a true physical association. There are other cluster merger candidates among our potential cluster catalog; however, many or most of them are likely line-of-sight projections (given the wide redshift slices). The *XMM*-LSS field has ongoing further spectroscopic coverage from the DEVILS survey (Davies et al. 2018) and will have even more extensive coverage from the planned PFS (Tamura et al. 2018) galaxy evolution survey. These will help us further disentangle the nature of the overdensity we find in our density maps.

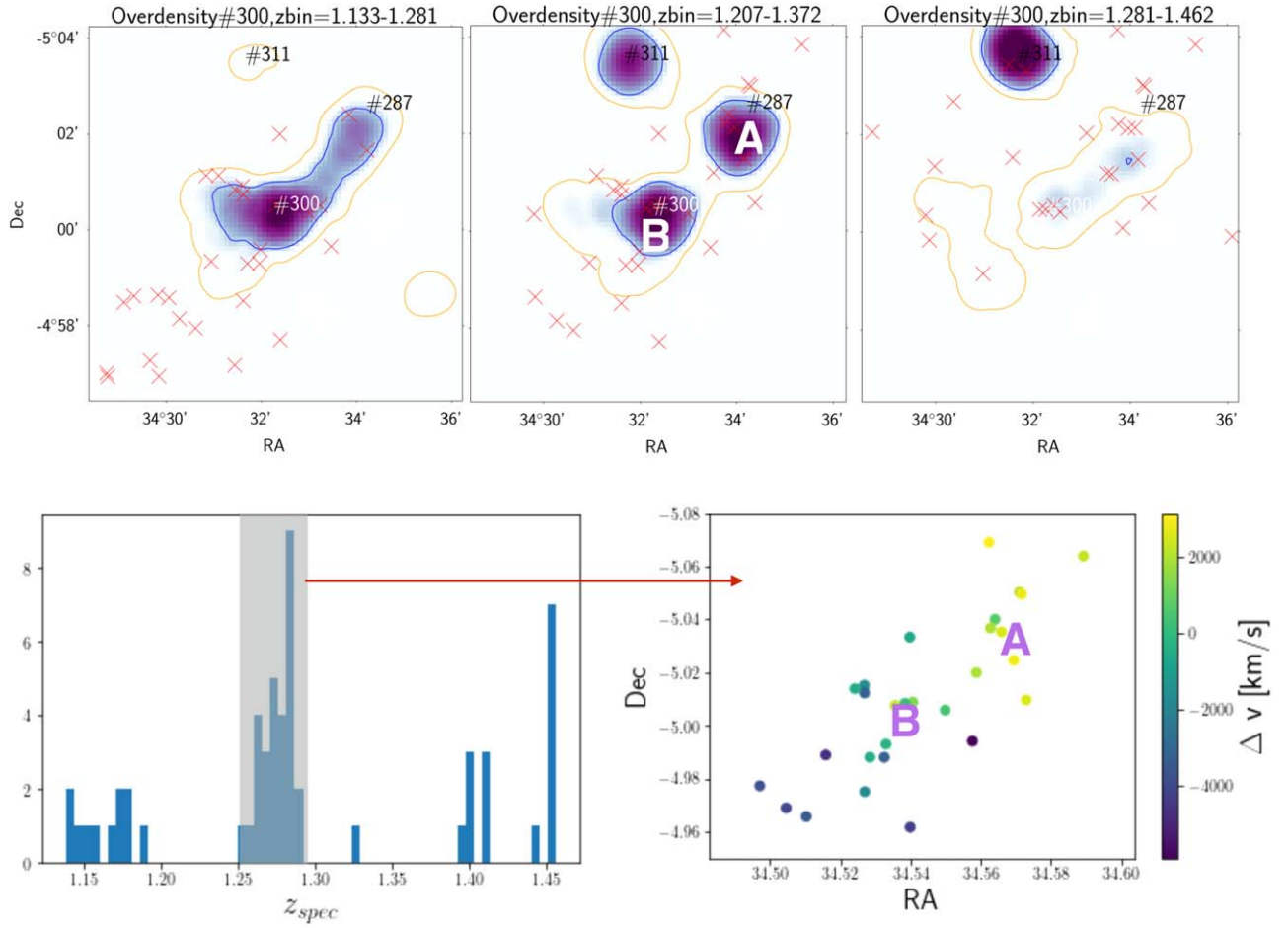


Figure 10. Potential new $z = 1.28$ cluster merger. The middle panel shows the peak density redshift slice for this structure, with the neighboring overlapping redshift slices shown on either side. The bottom left panel shows all available spectroscopic redshifts showing a clear peak at $z \sim 1.28$, corresponding to the middle of the peak density redshift slice. The bottom right panel shows that Component A is behind Component B in redshift space.

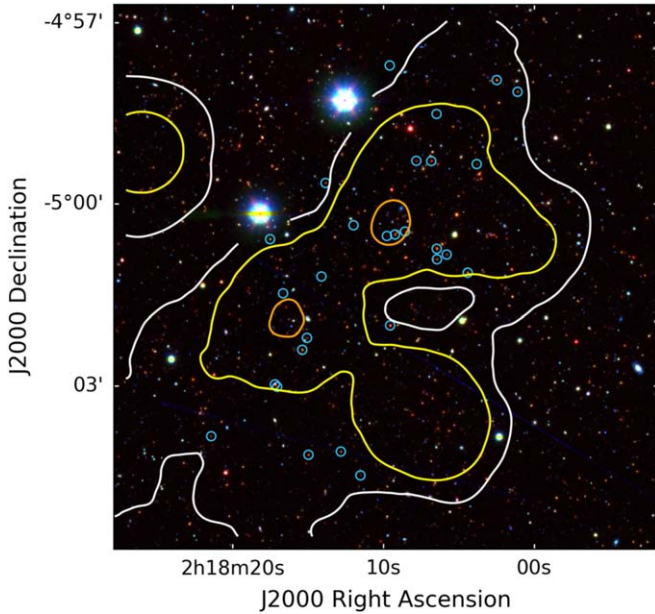


Figure 11. Three-color RGB image of the field of the $z = 1.28$ cluster merger, with contours of overdensity in the $1.207 < z < 1.372$ redshift slice as follows; 0.25 in white, 0.5 in yellow, and 1.0 in orange. The red channel is *Spitzer* IRAC 4.5 μm , the green channel the VIDEO H band, and the blue channel the HSC ultra-deep i band. Galaxies with spectroscopic $z \approx 1.28$ are marked with light-blue circles.

4. Summary and Conclusions

In this paper we present new photometric redshifts for the 4.8 deg^2 *XMM*-LSS field. We use them to compute surface density maps in the range $0.1 < z < 1.6$. We use a simulated light cone to assess the recoverability of true structures using such density maps. We summarize our key results as follows:

1. Photometric redshifts at the level of $\sigma(z)/(1+z) \approx 0.03$ allow us to recover dark matter halos with $\log(M_{\text{halo}}/M_{\odot}) \gtrsim 13.7$, as we show based on a comparison with a simulated light cone.
2. We construct 2D density maps for the *XMM*-LSS in 28 redshift slices covering $z = 0.1$ – 1.6 . These density maps show evidence of extended overdensities, visually similar to filaments, as well as compact overdensities likely associated with massive halos.
3. Using an evolving percentile mass density per comoving volume threshold that we determine from our simulated light cone, we find 339 halos with $\log(M_{\text{halo}}/M_{\odot}) > 13.7$ from $0.1 < z < 1.6$ and a peak of $z \sim 0.8$. Their number and redshift distribution are consistent with expectations from our simulated light cone.
4. Among our likely massive halo overdensities, we recover 43 of the 70 known spectroscopically confirmed X-ray clusters in the field (Adami et al. 2018). The unrecovered ones are predominantly below $z \sim 0.4$, where the X-ray

clusters tend to have lower masses than our target threshold.

5. We present some interesting case studies, including a potential massive evolved cluster at $z \sim 1.5$ and a potential cluster merger at $z \sim 1.28$.

This paper is proof of concept on the degree to which we can reliably probe both the local and large-scale environment of galaxies using photometric redshifts of the quality already achievable for moderately large area surveys such as SERVS. The next papers in the series will use these density maps to further quantify the presence of filaments and look at the role of local and large-scale environment on the growth of galaxies and their supermassive black holes.

The authors acknowledge useful discussions with Rachel Bezanson, Frank van den Bosch, and Eric Gawiser that helped guide our analysis. The authors especially thank Ryan Cybulski for providing his Voronoi Tessellation IDL code, which N.K. translated into python and has used for this project. B.D. acknowledges financial support from the National Science Foundation, grant No. 1716907.

Appendix Photometric Redshift Comparison

In this paper we use photometric redshifts based on the template fitting code EAZY as described in detail in the body of the paper. However, this may lead to a potential bias driven by the particular choice of templates. Our zero-point offset corrections are meant to mitigate such biases to some extent, but this correction is driven by the available spectroscopic redshifts, which represent a biased subset of the whole as shown in Figure 2. The HELP team performed a more sophisticated photometric redshift analysis in this field, considering several different template libraries and performing a hierarchical Bayesian analysis to find the best redshift overall. While this is clearly a more sophisticated approach, the downside for us is that that work uses the data fusion catalogs that adopt the single-band SExtractor IRAC photometry. However, we now have the Tractor forced photometry (Nyland et al. 2017), which is better at deblending IRAC sources, leading to more accurate results, especially at higher redshifts ($z > 1$).

In Figure 12, we show the direct comparison between our EAZY photometric redshifts and the HELP photometric redshifts.²⁹ This plot shows very good agreement in the range $0.3 < z < 1.0$ but also has significant deviations at either end outside this range. We performed the pair analysis for the HELP redshifts at those two ends—for the $z < 0.3$ bin and the $z > 1.2$ bin, we get $\sigma/(1+z)$ of 0.016 and 0.053, respectively. At the lower-redshift end, this is better than EAZY (see Figure 3), but in the higher-redshift bin this is much worse than EAZY, as expected given the effect of blended IRAC photometry therein. While there are clearly advantages and disadvantages to both approaches, we chose our EAZY redshifts for our analysis in particular because of this behavior at $z > 1$. This comparison highlights the significant biases that can exist between photometric redshifts derived based on different photometric catalogs and using different approaches. Therefore, we reemphasize that the list of overdensities we present here are only candidates. Their confirmation requires high spectroscopic completeness out to $z \sim 1.5$ as expected

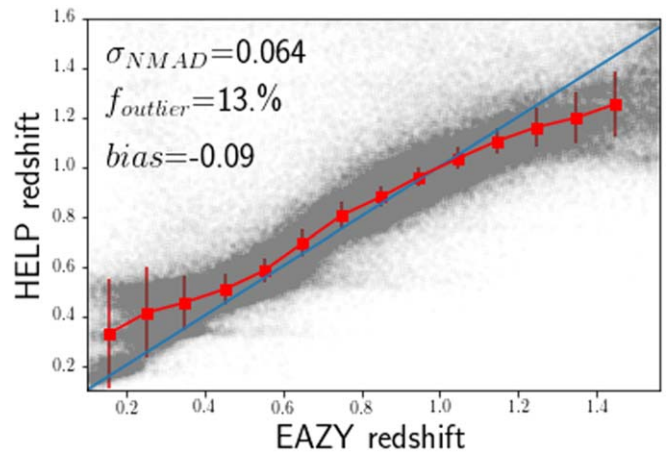


Figure 12. Comparison between the EAZY photometric redshifts adopted in this paper and the HELP photometric redshifts described in Duncan et al. (2018). The legend gives the statistics across the full range of interest ($0.1 < z < 1.6$), whereas the red symbols and error bars give the median values and σ_{NMAD} in bins of 0.1 in EAZY redshifts.

from the PFS galaxy evolution survey, which will include the XMM-LSS field (e.g., Tanaka et al. 2018).

ORCID iDs

Anna Sajina <https://orcid.org/0000-0002-1917-1200>
 Mark Lacy <https://orcid.org/0000-0002-3032-1783>
 Duncan Farrah <https://orcid.org/0000-0003-1748-2010>
 Behnam Darvish <https://orcid.org/0000-0003-4919-9017>
 Ken Duncan <https://orcid.org/0000-0001-6889-8388>
 Seb Oliver <https://orcid.org/0000-0001-7862-1032>

References

- Adami, C., Giles, P., Koulouridis, E., et al. 2018, *A&A*, **620**, A5
 Alam, S., Albareti, F. D., Allende Prieto, C., et al. 2015, *ApJS*, **219**, 12
 Baldry, I. K., Robotham, A. S. G., Hill, D. T., et al. 2010, *MNRAS*, **404**, 86
 Bradshaw, E. J., Almaini, O., Hartley, W. G., et al. 2013, *MNRAS*, **433**, 194
 Brammer, G. B., van Dokkum, P. G., & Coppi, P. 2008, *ApJ*, **686**, 1503
 Bremer, M. N., Valtchanov, I., Willis, J., et al. 2006, *MNRAS*, **371**, 1427
 Brodwin, M., Lilly, S. J., Porciani, C., et al. 2006, *ApJS*, **162**, 20
 Chen, C.-T. J., Brandt, W. N., Luo, B., et al. 2018, *MNRAS*, **478**, 2132
 Chiang, Y.-K., Overzier, R. A., Gebhardt, K., & Henriques, B. 2017, *ApJL*, **844**, L23
 Clerc, N., Adami, C., Lieu, M., et al. 2014, *MNRAS*, **444**, 2723
 Cochrane, R. K., & Best, P. N. 2018, *MNRAS*, **480**, 864
 Coil, A. L., Blanton, M. R., Burles, S. M., et al. 2011, *ApJ*, **741**, 8
 Cole, S., Lacey, C. G., Baugh, C. M., & Frenk, C. S. 2000, *MNRAS*, **319**, 168
 Cool, R. J., Moustakas, J., Blanton, M. R., et al. 2013, *ApJ*, **767**, 118
 Dahlen, T., Mobasher, B., Faber, S. M., et al. 2013, *ApJ*, **775**, 93
 Darvish, B., Mobasher, B., Sobral, D., Scoville, N., & Aragon-Calvo, M. 2015a, *ApJ*, **805**, 121
 Darvish, B., Mobasher, B., Sobral, D., et al. 2015b, *ApJ*, **814**, 84
 Davies, L. J. M., Robotham, A. S. G., Driver, S. P., et al. 2018, *MNRAS*, **480**, 768
 Dressler, A. 1980, *ApJ*, **236**, 351
 Duivenvoorden, S., Oliver, S., Buat, V., et al. 2016, *MNRAS*, **462**, 277
 Duncan, K. J., Brown, M. J. I., Williams, W. L., et al. 2018, *MNRAS*, **473**, 2655
 Etherington, J., Thomas, D., Maraston, C., et al. 2017, *MNRAS*, **466**, 228
 Guzzo, L., Scodreggio, M., Garilli, B., et al. 2014, *A&A*, **566**, A108
 Ilbert, O., Arnouts, S., McCracken, H. J., et al. 2006, *A&A*, **457**, 841
 Ilbert, O., McCracken, H. J., Le Fèvre, O., et al. 2013, *A&A*, **556**, A55
 Jarvis, M. J., Bonfield, D. G., Bruce, V. A., et al. 2013, *MNRAS*, **428**, 1281
 Lagos, C. d. P., Bayet, E., Baugh, C. M., et al. 2012, *MNRAS*, **426**, 2142
 Laigle, C., McCracken, H. J., Ilbert, O., et al. 2016, *ApJS*, **224**, 24
 Laigle, C., Pichon, C., Arnouts, S., et al. 2018, *MNRAS*, **474**, 5437

²⁹ We adopted the $z_{1\text{median}}$ redshifts from the HELP catalog, which is their recommended measure.

- Lang, D., Hogg, D. W., & Mykytyn, D. 2016, The Tractor: Probabilistic Astronomical Source Detection and Measurement, Astrophysics Source Code Library, ascl:1604.008
- Le Fèvre, O., Cassata, P., Cucciati, O., et al. 2013, *A&A*, **559**, A14
- Le Fèvre, O., Tasca, L. A. M., Cassata, P., et al. 2015, *A&A*, **576**, A79
- Lonsdale, C. J., Smith, H. E., Rowan-Robinson, M., et al. 2003, *PASP*, **115**, 897
- Madau, P., & Dickinson, M. 2014, *ARA&A*, **52**, 415
- Malavasi, N., Arnouts, S., Vibert, D., et al. 2017, *MNRAS*, **465**, 3817
- Mauduit, J.-C., Lacy, M., Farrah, D., et al. 2012, *PASP*, **124**, 714
- McLure, R. J., Pearce, H. J., Dunlop, J. S., et al. 2013, *MNRAS*, **428**, 1088
- McLure, R. J., Pentericci, L., Cimatti, A., et al. 2018, *MNRAS*, **479**, 25
- Merson, A. I., Baugh, C. M., Helly, J. C., et al. 2013, *MNRAS*, **429**, 556
- Moster, B. P., Somerville, R. S., Newman, J. A., & Rix, H.-W. 2011, *ApJ*, **731**, 113
- Muldrew, S. I., Croton, D. J., Skibba, R. A., et al. 2012, *MNRAS*, **419**, 2670
- Muzzin, A., Marchesini, D., van Dokkum, P. G., et al. 2009, *ApJ*, **701**, 1839
- Norberg, P., Baugh, C. M., Hawkins, E., et al. 2002, *MNRAS*, **332**, 827
- Nyland, K., Lacy, M., Sajina, A., et al. 2017, *ApJS*, **230**, 9
- Peng, Y.-j., Lilly, S. J., Kovač, K., et al. 2010, *ApJ*, **721**, 193
- Pentericci, L., McLure, R. J., Franzetti, P., et al. 2018, *A&A*, **616**, A174
- Pforr, J., Vaccari, M., Lacy, M., et al. 2019, *MNRAS*, **483**, 3168
- Planck Collaboration, Ade, P. A. R., Aghanim, N., et al. 2016, *A&A*, **594**, A13
- Quadri, R. F., & Williams, R. J. 2010, *ApJ*, **725**, 794
- Shirley, R., Roehlly, Y., Hurley, P. D., et al. 2019, *MNRAS*, **490**, 634
- Springel, V. 2005, *MNRAS*, **364**, 1105
- Springel, V., & Farrar, G. R. 2007, *MNRAS*, **380**, 911
- Tamura, N., Takato, N., Shimono, A., et al. 2018, *Proc. SPIE*, **10702**, 107021C
- Tanaka, M., Coupon, J., Hsieh, B.-C., et al. 2018, *PASJ*, **70**, SP1
- Vaccari, M. 2016, in The Universe of Digital Sky Surveys, ed. N. R. Napolitano et al., Vol. 42 (Cham: Springer), 71
- van Breukelen, C., Cotter, G., Rawlings, S., et al. 2007, *MNRAS*, **382**, 971
- van der Burg, R. F. J., Muzzin, A., Hoekstra, H., et al. 2013, *A&A*, **557**, A15
- Yamada, T., Nakamura, Y., Matsuda, Y., et al. 2012, *AJ*, **143**, 79
- Yang, G., Brandt, W. N., Darvish, B., et al. 2018, *MNRAS*, **480**, 1022
- Yuan, F., Lidman, C., Davis, T. M., et al. 2015, *MNRAS*, **452**, 3047